Remote Sensing of Environment 154 (2014) 387–397

Contents lists available at ScienceDirect

Remote Sensing of Environment

journal homepage: www.elsevier.com/locate/rse

Subcanopy Solar Radiation model: Predicting solar radiation across a heavily vegetated landscape using LiDAR and GIS solar radiation models

Collin A. Bode [a,*], Michael P. Limm [b], Mary E. Power [a], Jacques C. Finlay [c]

[a] Department of Integrative Biology, University of California, Berkeley, United States
[b] Biological Sciences, Holy Names University, United States
[c] Department of Ecology, Evolution and Behavior, University of Minnesota, United States

ARTICLE INFO

Article history:
Received 24 April 2013
Received in revised form 20 January 2014
Accepted 22 January 2014
Available online 26 April 2014

Keywords:
Solar model
Insolation
Irradiance
Radiative transfer
LiDAR
Subcanopy
Vegetation shading
Watershed
Angelo Reserve

ABSTRACT

Solar radiation flux, irradiance, is a fundamental driver of almost all hydrological and biological processes. Ecological models of these processes often require data at the watershed scale. GIS-based solar models that predict insolation at the watershed scale take topographic shading into account, but do not account for vegetative shading. Most methods that quantify subcanopy insolation do so only at a single point. Further, subcanopy model calibration requires significant field effort and knowledge of characteristics (species composition, leaf area index & mean leaf angle for each species), and upscaling to watersheds is a significant source of uncertainty.

We propose an approach to modeling insolation that uses airborne LiDAR data to estimate canopy openness as a Light Penetration Index (LPI). We couple LPI with the GRASS GIS r.sun solar model to produce the Subcanopy Solar Radiation model (SSR). SSR accounts for both topographic shading and vegetative shading at a landscape scale.

After calibrating the r.sun model to a weather station at our study site, we compare SSR model predictions to black thermopile pyranometer field measurements and to hemispherical photographs using Gap Light Analyzer software, a standard method for point estimation of subcanopy radiation. Both SSR and hemispherical models exhibit a similar linear relationship with pyranometer data, and the models predict similar total solar radiation flux across the range of canopy openness. This approach allows prediction of light regimes at watershed scales with resolution that was previously possible only for local point measurements.

Published by Elsevier Inc.

1. Introduction

Variation in solar radiation is a fundamental control over most physical, biogeochemical, and biological processes on Earth. Radiation flux governs temperature, a major control over air and water movements as well as biogeochemical cycling and physiological and ecological rates. Solar radiation is also a key energy source for photo-autotrophs. Where light is limiting, photo-autotrophs with adaptations for harvesting sparse photon fluxes can still persist in terrestrial (Chazdon & Pearcy, 1991; Pearcy, 1990) and aquatic (Falkowski & LaRoche, 2004; Glazer, 1985; Hill, 1996) environments. The ecological importance of light, even at low levels, requires that we measure it with high spatial and temporal resolution. Despite its importance, few studies have quantified variation in solar radiation below vegetation canopy across a landscape at spatial and temporal resolutions relevant to individual organisms, microclimates, or ecological processes.

The fraction of solar radiation reaching the ground or water surface is controlled by atmospheric conditions, topography, and vegetation. These factors have been assessed with both direct and indirect measurement methods. Direct methods use individual sensors or sensor arrays to quantify radiation (e.g. total solar energy, heat, or photosynthetically active radiation (PAR)). Sensors are placed under different types of vegetation at many locations to quantify spatial and temporal variability over some time period. There is a high level of inherent microsite variability in direct subcanopy measurements. Aggregating time or increasing the number of instruments can reduce the uncertainty due to high natural variability (Link, Marks, & Hardy, 2004). Results can be upscaled using a vegetation distribution map (Julian, Stanley, & Doyle, 2008).

Indirect measurement methods characterize the canopy and topography at a location, then model light transmission. A densiometer or hemispherical photograph is used to quantify canopy and topography in the hemisphere of sky directly above and around the observer. This hemisphere is gridded into sky region (Anderson, 1964; Frazer, Fournier, Trofymow, & Hall, 2001). These sky regions are then analyzed using software, such as Gap Light Analyzer (GLA), to predict canopy openness, and daily mean solar radiation (Frazer & Canham,1999). Sky regions have been used to estimate red:far red ratio (Lakso, 1980), leaf area index (Rich, 1990) and seasonal changes in canopy characteristics (Archibold & Ripley, 2004). Solar radiation estimates from hemispherical photographs have been related to plant growth (Canham, 1988;

* Corresponding author at: 1005 VLSB #1096, University of California, Berkeley, Berkeley, CA94720-1096, United States. Tel.: +1 415 305 5346.
E-mail address: collin@berkeley.edu (C.A. Bode).

http://dx.doi.org/10.1016/j.rse.2014.01.028
0034-4257/Published by Elsevier Inc.

Pearcy, 1983), flowering and fruit ripening (Lakso, 1980), leaf carbon isotope ratios (Ehleringer, Field, Lin, & Kuo, 1986), and snow melt (Hardy et al., 2004; Pomeroy et al., 2008; Reid, Essery, Rutter, & King, 2013).

While these direct and indirect methods quantify light environments, they have potential shortcomings. Under forest canopy, brief periods of direct insolation (sunflecks) can dominate daily and seasonal solar radiation input (Chazdon & Pearcy, 1991). Sensors separated by less than a meter can record a three-fold difference in photon flux density (Chazdon, Williams, & Field, 1988), and this local variability may introduce significant error when a limited number of measurements are used to estimate solar radiation flux over a large scale. Temporally, it may be difficult to upscale instantaneous (or daily averaged) values to monthly or annual totals due to seasonal changes in sun position (Canham, 1988) and leaf-emergence or leaf-fall (Hill, 1996). In addition, daily physical conditions may limit sampling and analysis. For example, hemispherical photographs are best taken in indirect light (full clouds or dawn/dusk). Full sunlight can reduce canopy information on the sensor (film or digital camera), distorting canopy openness estimates. Methods applying Beer's Law require leaf area index, leaf angle for each species and require an accurate species composition map (Canham, 1988; Gendron, Messier, & Comeau, 1998). While this is a reasonable approach in relatively homogenous forest stands, it is impractical in natural, heterogeneous systems, especially those with extensive riparian areas where species diversity is high. These methods require considerable ground effort to accurately characterize light environments at a high resolution across a landscape (Finlay, 2011).

Light modeling at the landscape scale requires Geographical Information Systems (GIS) based solar models. GIS solar models operate on digital elevation model (DEM) raster layers, allowing them to accurately estimate insolation reduction due to slope and aspect and topographic shading across watersheds (Dozier & Frew, 1990). ESRI's ArcGIS Solar Analyst refined the technique by adapting the sky region technique used in hemispherical photos for use with raster grids (Fu & Rich, 2000). R.sun introduced scaling methods to handle very large datasets (Hofierka & Suri, 2002). While GIS models address orographic shading, none are designed to account for vegetation. Until recently, spatially extensive measurements were not detailed enough to resolve vegetation effects (Hudak, Evans, & Smith, 2009).

Airborne LiDAR (Light Detection And Ranging) can now provide critical structural detail on vegetation that we previously lacked (Slatton, Carter, Shrestha, & Dietrich, 2007). LiDAR has been used to investigate vegetation characteristics, including canopy height (Anderson et al., 2006; Magnussen & Boudewyn, 1998; Nęsset, 1997). It has also been applied to leaf area index and above ground biomass (Boudreau et al., 2008; Drake, Dubayah, Knox, Clark, & Blair, 2002; Hurtt et al., 2004; Hyde et al., 2006; Lefsky et al., 1999; Næsset & Gobakken, 2008) and forest 3-dimensional structure (J. Anderson et al., 2006). Leaf-on and leaf-off LiDAR has been assessed for both canopy height and fractional canopy cover in riparian areas (Wasser, Day, Chasmer, & Taylor, 2013). LiDAR has been applied to subcanopy shading using the point cloud to predict shade levels at different times of day (Lee, Slatton, Roth, & Cropper, 2009).

Our goal in this paper was to integrate available tools including LIDAR to model solar radiation for heavily vegetated watersheds underneath the canopy. Our target habitat has diverse vegetation with heterogeneous, perhaps unknown, size and spatial structure. We propose an approach to modeling insolation, termed the Subcanopy Solar Radiation model (SSR), that uses a GIS based solar model coupled with a LiDAR-derived index of canopy openness to account for both topographic and vegetative shading. We apply this method to an 8 km × 8 km area encompassing rugged terrain, diverse terrestrial habitats and 3 small watersheds. To validate the approach, we apply both direct and indirect point methods (black thermopile pyranometer measurements, hemispherical photographs analyzed with Gap Light Analyzer) to our study site and compare them to the Subcanopy Solar Radiation model output.

2. Methods

2.1. Site

Our study sites are in the upper basin of the South Fork Eel River within the Heath and Marjorie Angelo Coast Range Reserve in Mendocino County, California (Fig. 1). The Angelo Reserve, in the University of California Natural Reserve System, has rugged, steep ridge-valley topography. Elevation ranges from 400 m to 1420 m within the Reserve. The region has a Mediterranean climate with wet, cool winters and warm, dry summers. For the purposes of this study, vegetation in the watershed can be broadly classified into four major plant communities: conifers, mixed-hardwood, chaparral, and meadow. The conifer assemblage consists of old-growth Douglas fir (*Pseudotsuga menziesii*) and redwood (*Sequoia sempervirens*). The mixed-hardwood includes several oaks (*Lithocarpus densiflorus*, *Quercus agrifolia*, *Q. kelloggi*), California bay (*Umbellularia californica*), and madrone (*Arbutus menziesii*). Chaparral is dominated by several species of manzanita (*Arctostaphlos manzanita*, *A. columbiana*, *A. glandulosa*). The meadows host native perennial grasses, European annual grasses, and native and exotic forbs (Suttle, Thomsen, & Power, 2007).

We have 3 nested spatial scales to our study sites. To capture orographic effects of shading, we included steep east and west ridges of the local terrain. This area produces an 8 km × 8 km square. We used the 2004 LiDAR dataset described below. Within this area we examined radiative transfer through vegetation, with higher resolution LiDAR from 2009 at 3 km × 6 km. Finally, our validation datasets used 26 point locations, including a weather station, within the study area (Fig. 1).

2.2. LiDAR data collection

Two leaf-on Airborne LiDAR datasets (2004, 2009) were used in this study. Both were collected by the National Center for Airborne Laser Mapping (http://www.ncalm.org) and are archived at OpenTopography.org. The first survey was flown in June 27–30, 2004 and covered the headwaters of the South Fork Eel river (Fig. 1, Table 1, DOI: 10.5069/G9639MPN). First returns were used to construct the canopy digital elevation model (DEM) and last returns were used to construct bare-earth DEM. The second survey was flown in September 4–7, 2009 on a narrow swath 0.5 km to either side of the South Fork Eel river main stem (Fig. 1, Table 1, DOI: 10.5069/G93F4MH1). First, second, third, and last returns were collected. Only last returns were used from the 2009 dataset for vegetation structure analysis.

Both LiDAR datasets were classified into ground and non-ground returns by NCALM using TerraScan (TerraSolid Ltd., Finland) each producing two point clouds: filtered (ground) and unfiltered (both ground and non-ground) using a TIN densification filter (Axelsson, 1999), see Fig. 5a below. Each point has a location (X, Y), laser intensity, and several returns at varying elevations. The 2004 point cloud was processed into bare-earth and canopy DEMs. 1 m bare-earthDEM was produced by kriging the ground filtered point cloud using Surfer (Golden Software Inc.), then was resampled to 2 m cell size. We developed a 2 m canopy DEM using an algorithm that took the maximum unfiltered point within each cell as the canopy top. Manual post-processing removed hits on flying birds and other errors. By subtracting canopy elevation from bare-earth elevation, we derived a vegetation height map (Fig. 2). The ground filtered and total point clouds from the 2009 dataset were imported into GRASS and converted into 2 m raster grids of density (point counts per 4 m^2 cell).

2.3. Scale dependence issues with LiDAR data

LiDAR data densities present computational challenges for solar models. Many GIS functions will fail on a very large raster layer, but can be run on tiled subsets of the raster. This makes them scale

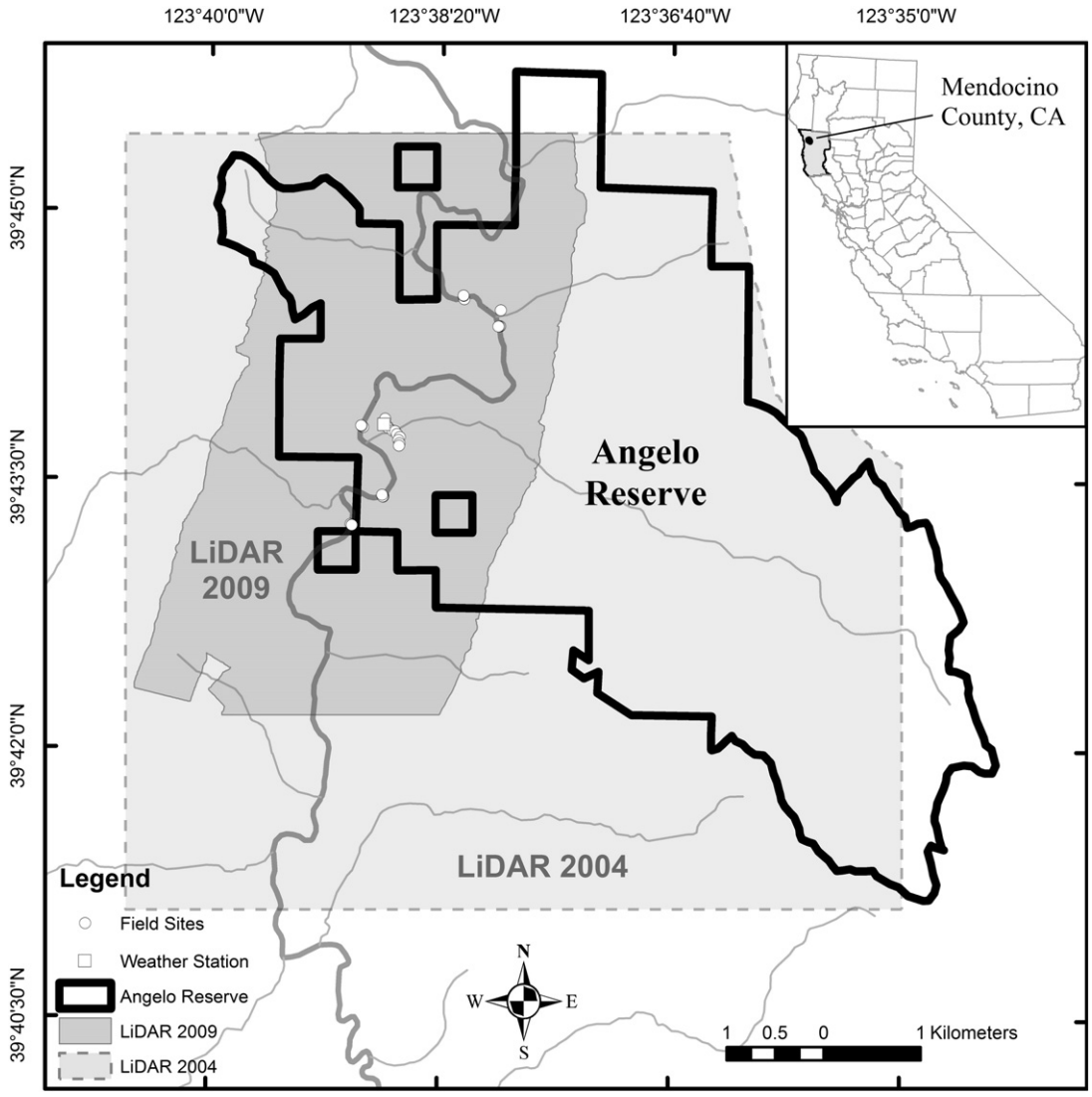

Fig. 1. Location of the Angelo Reserve, LiDAR 2004 & 2009 datasets, sample sites, and weather station. The weather station is used as a reference point in subsequent maps.

independent. Processing time increases linearly with dataset size. Solar models, on the other hand, are highly scale dependent. To properly calculate topographic shading, a solar model requires data for all mountains that block sunlight to the target area, even if they are kilometers away. Our study area, for example, included an 8 km × 8 km square necessary to capture the relevant ridgelines. At 2 m cell resolution this produced a raster with 16 million cells. Not being able to tile the data increases CPU, RAM, and Disk I/O intensity in a non-linear fashion. The high RAM requirements (~16 GB per process) make the use of high performance computing clusters impractical, as they do not have enough RAM per node (~2 GB RAM/node). As a result, we used a single Linux compute-workstation with 8 CPU cores and 96 GB of ram. We tested several solar models, but most could not open or process rasters larger than 2 million cells. ESRI's ArcGIS and its solar model, Solar Analyst, functioned on raster layers of up to 4 million cells before failing. We chose the open-sourceGRASS for GIS processing because it is designed to handle large datasets (http://grass.osgeo.org). GRASS successfully processed our 16 million cell rasters.

Table 1
LiDAR survey specifications.

	2004 LiDAR	2009 LiDAR
Flight dates	June 27–30, 2004	September 4–7, 2009
Sensor	Optech 2033	Optech GEMINI
Scan angle (cutoff)	±20° (±17°)	±21° (±18°)
Average flying height	600 m	800 m
Pulse rate frequency	33.3 kHz	100 kHz
Swath overlap	50%	50%
Returns collected	First, last	First, 2nd, 3rd, last
Point density	2.64 points/m^2	9.64 points/m^2
Total area	236 km^2	371 km^2
Area used in study	59.2 km^2	19.3 km^2

2.4. GRASS r.sun light model

GRASS GIS r.sun, is a clear sky solar model designed to take topographic angles and shading into account (Hofierka & Suri, 2002). Clouds are considered "real-sky" conditions, instead of "clear-sky" and increase the complexity of the model considerably, hence are left out. The model has only 4 inputs: digital elevation model (DEM), Julian Day, time-step, and Linke Turbidity Index. Linke Turbidity Index (T_L) is a single value aggregating non-cloud atmospheric conditions (Remund, Wald, LefÈvre, Ranchin, & Page, 2003). We used the 2004 LiDAR dataset for the r.sun model. Both the standard bare-earth and the canopy DEM were run through the model. The r.sun model will output one layer for a given Julian Day (1–365). R.sun operates on a user-definedtime-step, default 15 min, in our study set to 6 min. Individual time-steps of irradiance are aggregated to a 24 h insolation total in Wh/m^2. To produce a time-

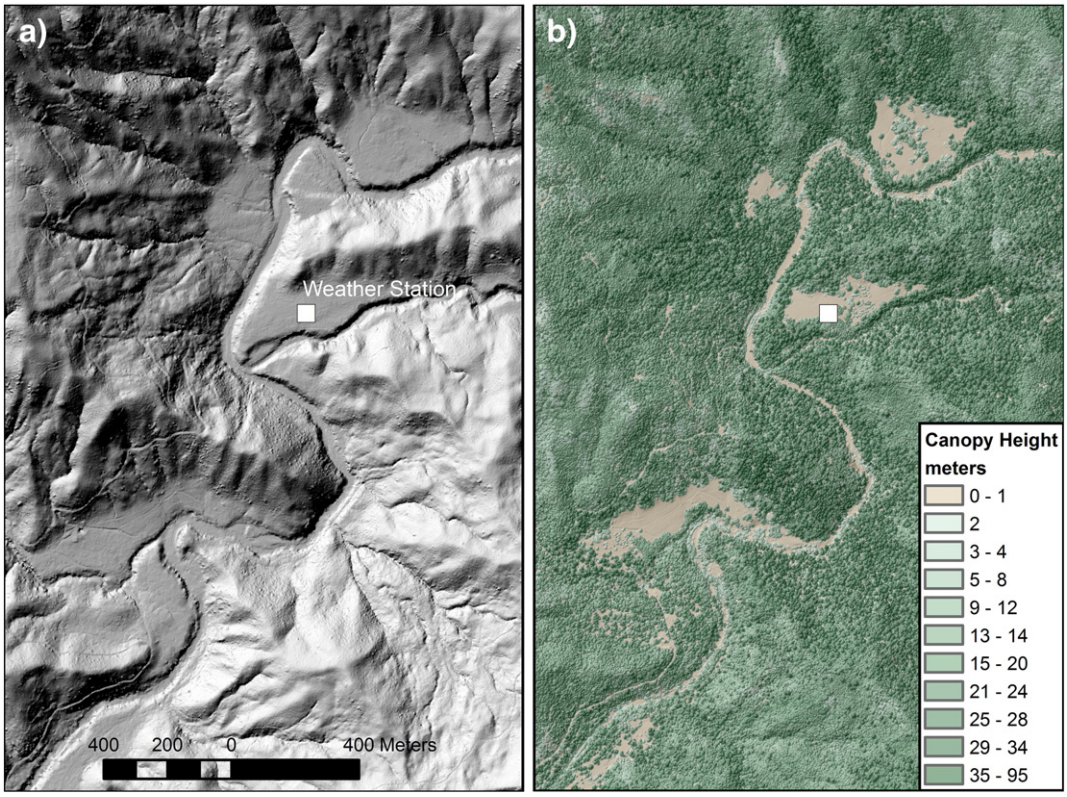

Fig. 2. Maps illustrating a) bare-earth filtered LiDAR hillshade, b) canopy filtered LiDAR colored by vegetation height for the study site.

series of light map layers, we developed a set of scripts in Python (http://www.python.org). Code can be downloaded from our public repository (https://github.com/cbode/ssr/). We chose to run the model once a week for the entire year. The weekly time-step was chosen to produce ecologically meaningful differences between layers without losing critical temporal resolution.

Linke Turbidity Index values, (T_L), were retrieved from the HelioClim project website (Helioclim, 2011), which has a satellite derived global database of T_L. We used linear interpolation to derive weekly values from the monthly dataset. T_L ranges from a minimum of 1.0 (very clear) to a maximum of 8.0 (very hazy). Angelo Reserve values ranged from 2.9 (Dec) to 3.8 (July).

The r.sun model calculates direct, and diffuse, and reflected shortwave radiation. In addition it produces global (direct + diffuse + reflected) radiation (Fig. 3). Ray-tracing is used for direct and reflected radiation, while diffuse radiation uses isotropic radiation based on the amount of sky visible (Šúri & Hofierka, 2004). Surface-reflected radiation does not exist in the understory, so we excluded reflection from our subcanopy model, but it is included in the gap model. For each day calculated we received 4 layers per DEM. With 2 DEMs (bare-earth, canopy) and 52 runs (weekly), 416 map layers were produced from the 2004 dataset.

2.4.1. GRASS r.sun calibration

We calibrated the r.sun model using our weather station and portable field pyranometers (Hukseflux LP02) at the Angelo Reserve. We picked a clear sky day with zero cloud cover (Aug 25, 2011). The r.sun global radiation was within 5% of the portable field pyranometer and weather station sensor (Fig. 4). However, r.sun assumes 20% diffuse radiation for our level of atmospheric turbidity (T_L) where our measurements showed only 10% diffuse radiation. A permanent solar monitoring site at Humboldt State University, 130 km north of the Angelo Reserve, also shows 10% diffuse radiation for the same time period (MIDC, 2013), suggesting that our measurements were accurate. No adjustment of the model parameters would get both the global and the diffuse outputs to match measured values. Therefore, we included a calibration adjustment by multiplying the diffuse radiation output by 0.50. The rest of the model has no empirical calibration.

2.5. Subcanopy Solar Radiation model (SSR)

The SSR model estimates subcanopy radiation at the watershed scale. For light modeling, we used the GRASS GIS r.sun. To calculate light levels underneath vegetation, we used the LiDAR point clouds. Instead of using the point cloud to indicate obstructions to light, as has been done in previous studies (Lee et al., 2009; Mücke & Hollaus, 2011), we used the LiDAR to indicate the probability of light reaching the ground, by using the laser as a proxy for beams of direct sunlight hitting the forest floor. This probability is estimated by the Light Penetration Index (LPI) = (Ground Hits) / (Total Hits) (Fig. 5) see also (Barilotti, 2006). The understory sub-model, described below, applies the LPI to both direct and diffuse radiation, producing layers of understory global radiation (watt-hours/m^2). The understory sub-model tends to blur edges, such as stream channels, meadow edges, and large individual trees. Blurring is caused by the neighborhood analysis function used to create the LPI, as explained below in Section 2.5.1. To model edges better, we developed a sub-model for large open gaps. A gap is defined here as one or more contiguous 2 m cells where the maximum vegetation height is lower than 2 m. SSR is the combination of the two sub-models. Each component will be described further below.

2.5.1. Light penetration index (LPI)

To assess canopy openness, we developed the Light Penetration Index (LPI) from LiDAR point cloud data. LPI is an index of the probability that a direct beam of light will penetrate the vegetation and hit the ground (Fig. 5b). Sunlight penetrates vegetation at changing angles throughout the day. Fortuitously, the scan angles of the laser beam from the LiDAR sweep a swath left and right, perpendicular to the

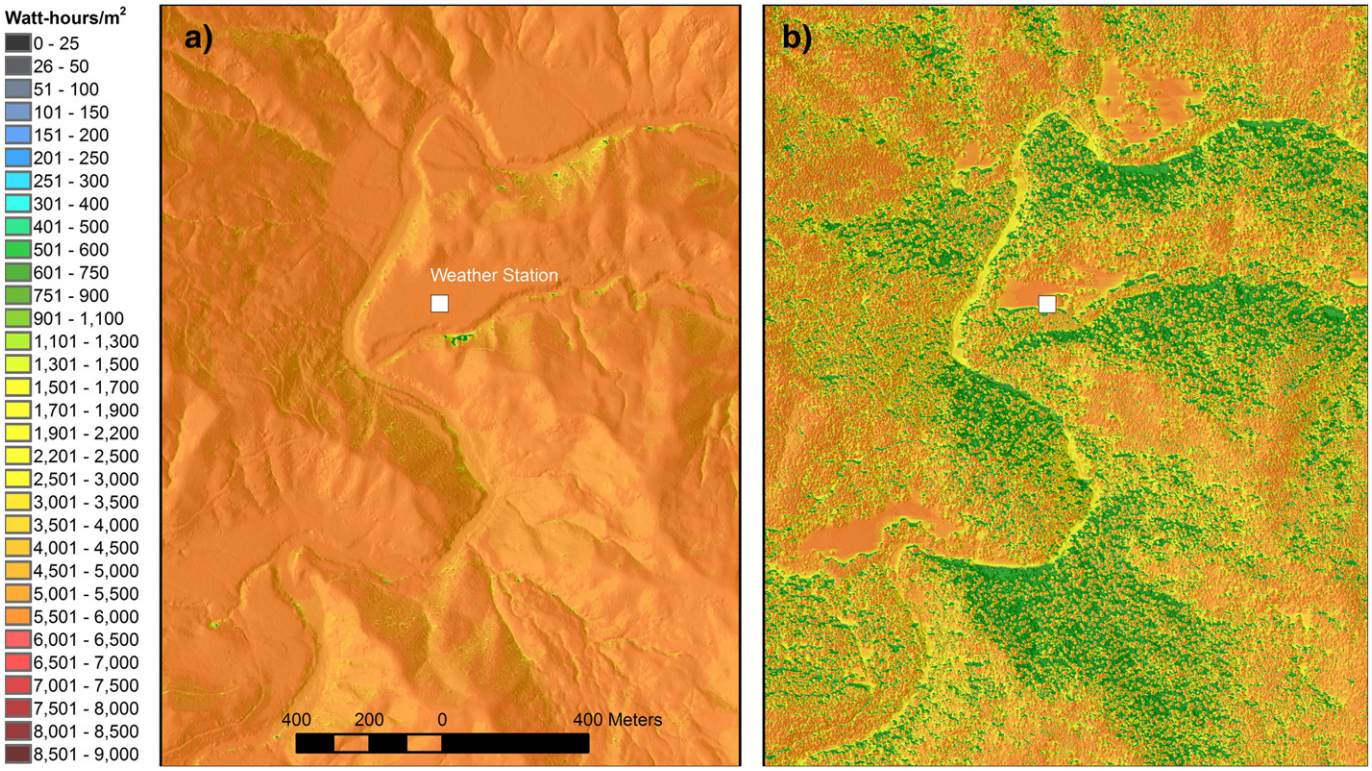

Fig. 3. GRASS GIS r.sun global output a) bare-earth, b) canopy. Values are scaled from peak summer insolation to minimum winter insolation.

forward path of the aircraft. This swath causes laser beams to hit targets on the ground or canopy surfaces with a range of angles which can be equated roughly with the way sunlight hits these surfaces (Fig. 6). The characteristics of the LiDAR sweep allow us to use aggregates of the LiDAR points to represent sunlight penetration from angles other than vertical.

We adjusted for diel changes in solar angle. To integrate the influence of neighboring vegetation as the solar angle changes throughout the day, we used a GIS function, neighborhood analysis (Shapiro, 2010). Neighborhood analysis is a moving window which sums all points within a square around each target cell. This will smooth the data spatially, because each cell will aggregate similar data as the cell next to it. Neighborhood analysis accounts for the shading caused by vegetation in nearby locations. The maximum obstructing distance (d) is the diameter of the neighborhood analysis, and is the distance away from a target location where vegetation would obstruct significant amounts of sunlight from reaching the location. This value can be derived as a statistical fit to measurements (Musselman, Margulis, & Molotch, 2013). To minimize local calibration of the model, we derived maximum obstructing distance using the fortuitous correspondence between natural sun beams and LiDAR swath angles. We computed the modal height of trees and bushes within our study area ($h = 22$ m). With scan angle (Table 1, 2009 scan angle = 18°) and tree height, we found the maximum obstructing distance (d) for the LiDAR beam would be 7.14 m (Eq. 1 and Fig. 7).

$$d = h/\tan\theta, \theta = (90^{\circ} - 18^{\circ}). \quad (1)$$

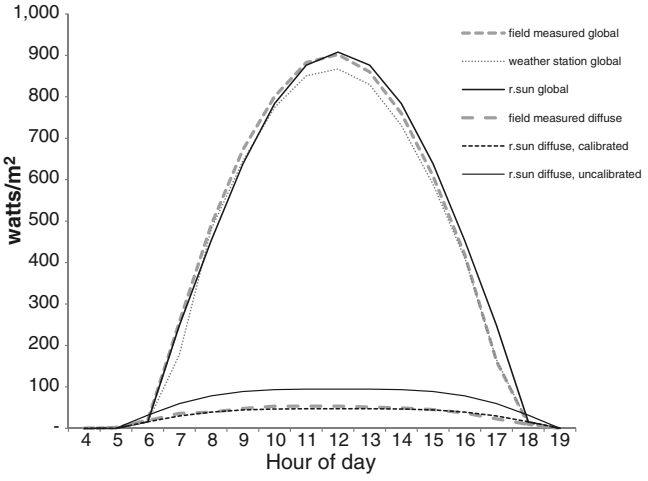

Fig. 4. Hourly output on August 25, 2011 of weather station, field sensor global, r.sun global, field sensor diffuse, and r.sun diffuse. Note the doubling of r.sun diffuse radiation.

Our raster resolution is 2 m cells, so the maximum obstructing distance (7.14 m) translates to 8 m. The GIS neighborhood analysis (i.e. r.neighbors) operates in a square around the target cell. Our square is 18 m × 18 m, because we have 8 m obstructing distance per side (16 m) plus a 2 m center cell (Fig. 8). All LiDAR points for ground and total are summed within the aggregation square and the ratio is assigned to the target square as LPI.

We also compensated for seasonal shifts in solar noon. Solar noon is the point in the sky where the sun is at the greatest angle from the horizon. In the northern hemisphere, when the sun is at summer solstice (in June), the neighborhood analysis square is roughly centered on its target cell. As the season progresses from June to December, the model moves the square south relative to the target cell, matching the sun angle at solar noon (σ). From December to June, the square moves northward relative to the target cell. This adjustment would be inverted for the southern hemisphere. Angelo Reserve is at 39.5°N latitude, giving it a solar noon from $\sigma = 73.1°$ at summer solstice to $\sigma = 27.3°$ at winter solstice (SOLPOS, 2012). The offset of the aggregation square can be defined as the maximum obstructing distance (d) multiplied by one minus the cosine of solar noon for the number of cells north (C_{north})

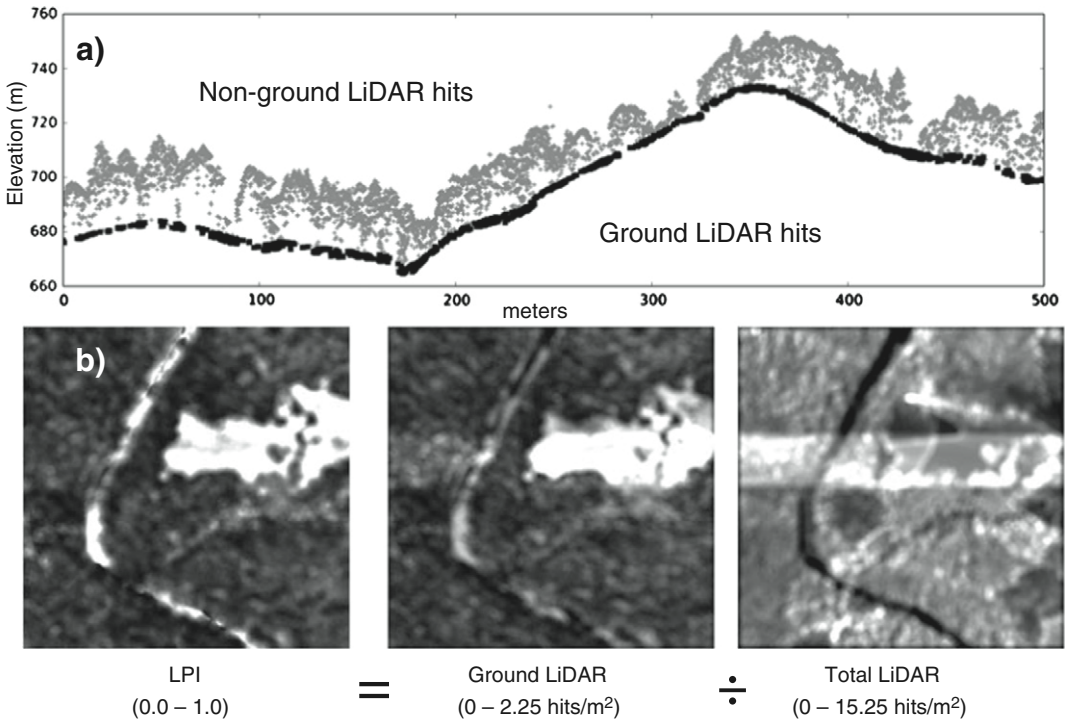

Fig. 5. a) Ground vs. non-ground LiDAR points. Ground points (black) and non-ground points (gray) in profile along a transect. Total hits is the combination of these two datasets. b) Map of LPI showing it as a ratio of ground hits to total hits.

of the target square (Eq. 2). C_{south} is the number of cells south of the target square (Eq. 3). C_{east} and $C_{west} = d$ represent diurnal variation and do not change seasonally.

$$C_{north} = d(1 - \cos\sigma) \quad (2)$$

$$C_{south} = d(1 + \cos\sigma). \quad (3)$$

The square sizes are rounded to the nearest 2 m cell and are shifted monthly, providing 4 seasonal shifts for LPI (Fig. 8). Using seasonal shifts allows us to refine LPI without being burdened by the computational load of ray-tracing through the point cloud. In contiguous forest stands seasonal shift would be unnecessary. It is valuable for edges and transitions, such as species transitions, riparian areas, and meadows. A

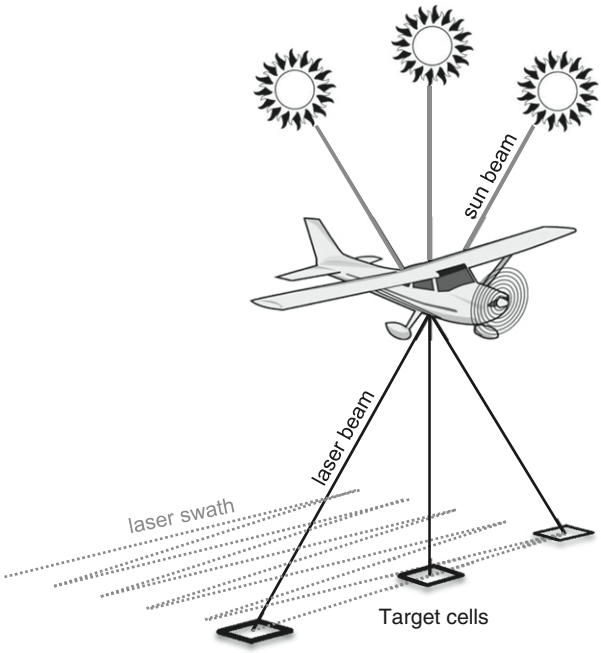

Fig. 6. Correlation between daily sun angles and LiDAR scan angles. LiDAR can only be a rough proxy for sunlight, since the airplane flight-lines do not match the path of the sun.

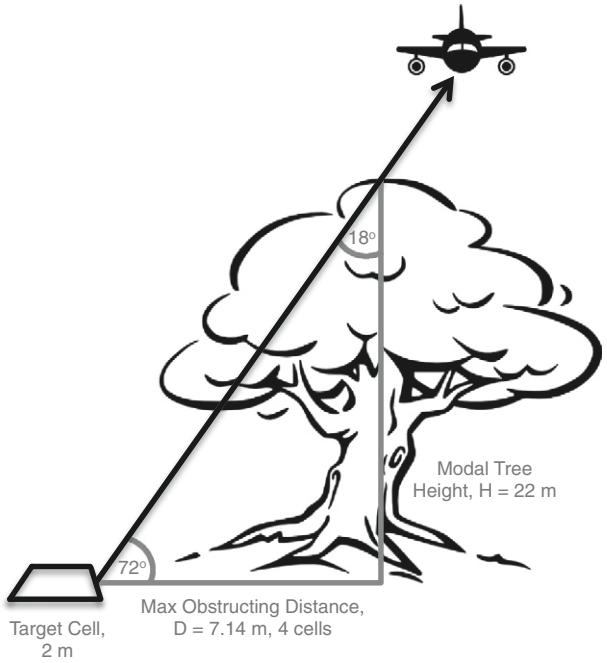

Fig. 7. Maximum obstructing distance of vegetation is a function of the height of the neighboring vegetation and the scan angle of the laser. For sunlight this would be infinite, since the sun sets at the horizon, but using the LiDAR scan angle provides a practical starting point.

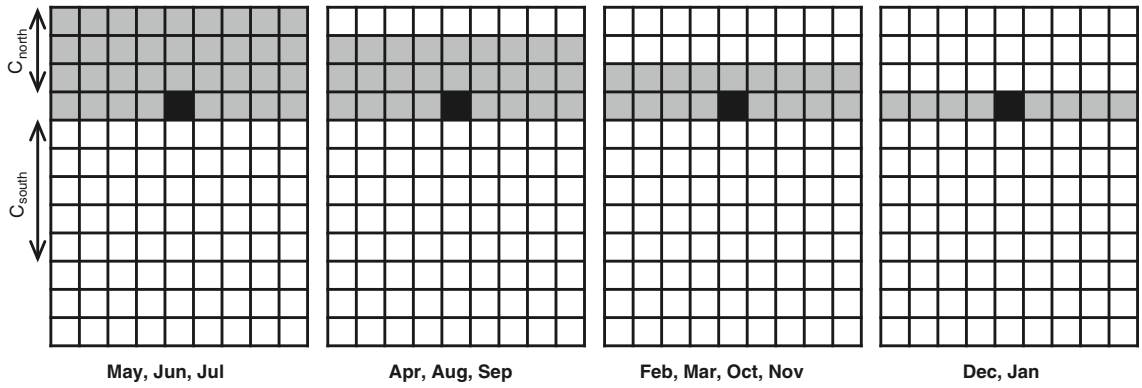

Fig. 8. Seasonal shift in neighborhood analysis square around the target cell based on the angle of solar noon. Black cell is the target cell. Gray cells are the neighborhood analysis square. C_{north} is the cell count to the northern boundary of the square. C_{south} is the cell count to the southern boundary of the square.

meadow may have a different species mix on its north side compared to its south side due to differing seasonal light regimes.

2.5.2. Understory sub-model

The Understory component combines the LPI with bare-earth r.sun output. Bare-earth is used because we are modeling light penetrating to the ground underneath the forest vegetation. The LPI provides attenuation of light due to the vegetation. Direct and diffuse radiation are calculated separately then combined into global subcanopy insolation (Eq. 4).

$$Global_{under} = Dir_{under} + Diff_{under}. \quad (4)$$

We use LPI without modification to produce understory insolation (Dir_{under}), since LPI is a measure of the probability of direct light hitting the forest floor (Eq. 5).

$$Dir_{under} = LPI \times Dir_{above}. \quad (5)$$

Direct r.sun output can be considered above canopy insolation (Dir_{above}). Diffuse radiation penetrates vegetation better than direct radiation, but despite the extensive studies on light flecks and subcanopy light, diffuse light remains a difficult value to quantify (Pearcy, 1990). The issue is further complicated by selective absorption of photosynthetically active radiation (400–700 nm) by plants. While we have some indications that the extinction rate is nonlinear, we decided to keep our model simple and uncalibrated. Experimentation with calibrated methods did not improve the results enough to warrant splitting our pyranometer measurements into a calibration and validation datasets. We used a simple linear regression predicting diffuse understory light from diffuse canopy light (Eq. 6) (Gendron et al., 1998). This is the only calibration used in the model other than the 0.5 multiplier on diffuse radiation in r.sun. Fig. 9a shows Understory output.

$$Diff_{under} = 1.024 \times LPI \times Diff_{above} + 0.01719. \quad (6)$$

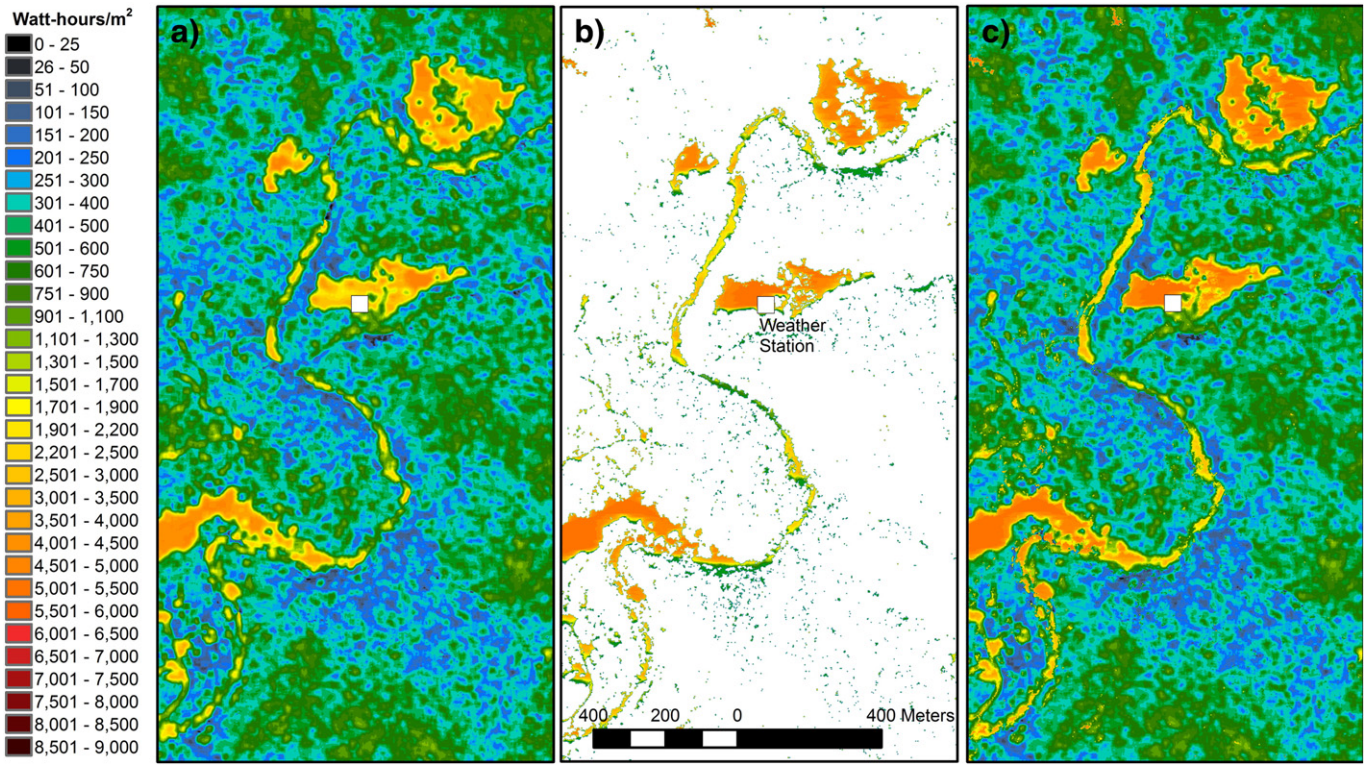

Fig. 9. SSR components: a) understory, b) gap (colored areas), and c) final SSR.

2.5.3. Gap sub-model

The Gap sub-model estimates insolation for edges and open areas. The Gap sub-model runs the r.sun light model on the canopy DEM, instead of the bare-earth DEM. R.sun parameters are otherwise identical to bare-earth model runs. LPI is not used in the Gap sub-model. R.sun treats the treetop canopy as if areas between canopy hits are solid: the trees are small stone mountains, producing highly detailed shadows. The goal of the model is to estimate insolation at the ground level in open areas. All cells covered by vegetation higher than 2 m are set to null, i.e. removed from the output. The 2 m height is a user-specified parameter and should be adjusted as appropriate to the study site. The resulting Gap sub-model layers estimate insolation with detailed tree shading (Fig. 9b). This captures narrow stream channels, individual tree shading, sharp vegetation ecotones, and other edges. Gap output will underestimate the insolation in shaded areas, because there is no algorithm to allow direct sunlight to pass through obstructing vegetation.

2.5.4. SSR

SSR is a simple combination of the Understory and Gap layers to provide a complete subcanopy radiation output. Using map algebra (Shapiro & Clements, 2010), for every cell in the layer, Understory and Gap are compared. The higher value is chosen as the final SSR value for global insolation (Eq. 7). For example, consider a large oak tree in the middle of a meadow, with a loose open canopy. Light measurements would show the area of a cell on the north side of the tree as receiving significant direct radiation due to light penetration through the canopy. The Gap sub-model would show that same cell as getting only diffuse light and no direct sunlight. In this circumstance, the Understory sub-model would be more accurate than the Gap sub-model, despite the cell being less than 2 m in an open field. To address this, SSR compares output of the two sub-models on a cell-by-cell basis and accepts the higher radiation value as the final output (Fig. 9c).

$$SSR = \max\left(Global_{under}, Global_{gap}\right). \quad (7)$$

2.6. Validation measurements: pyranometers & hemispherical photographs

To validate the SSR model, we used direct and indirect field measurements. For direct measurements, we used 2 pyranometers measuring global and diffuse radiation. For indirect measurements, we used hemispherical photographs and Gap Light Analyzer (GLA) software (Frazer & Canham, 1999). We made measurements at 26 sites across a range of canopy and topography conditions. The measurements were taken between August 26 and November 2, 2011. We used black thermopile based Hukseflux LP02 pyranometers, because silicon-based pyranometers are calibrated for direct sunlight and perform erratically under tree shade (Vignola, Stoffel, & Michalsky, 2012). To capture both direct and diffuse radiation, we used two pyranometers, one with a shade ring. We are aware that the high level of microsite variation decreases the value of a single set of direct measurements per site (Link et al., 2004). To significantly improve the sampling would have required 8 pyranometers, which was beyond our means. We recorded global and diffuse radiation and derived direct radiation. The shade ring was oriented so that the sensor would not receive any direct sunlight at any time and was placed north of the global sensor to prevent accidental shading. Sensors were leveled with a bubble-level, connected to a Campbell CR1000 datalogger and placed at 1 m height above ground on tripods. Each location was measured for at least 24 h, with the clearest contiguous 24 h used for estimates. Measurements were logged at 5 minute intervals as average irradiance (W/m^2). Data were aggregated to hourly averages for comparison with r.sun and summed to a 24 h period as Wh/m^2 for validation of SSR.

We performed indirect measurements using hemispherical photographs. Hemispherical photographic analysis has four steps: take a photograph, get the location and orientation of the photograph, manipulate the image to estimate canopy openness, and simulate sun flyover to estimate photon flux density through the different sky regions (Chazdon & Field, 1987; G. C. Evans & Coombe, 1959; Frazer et al., 2001; Rich, 1990). We used a fish-eye lens (4.5 mm focal length, Sigma Corp.) with an 180° field of view to capture hemispherical canopy photographs. The lens

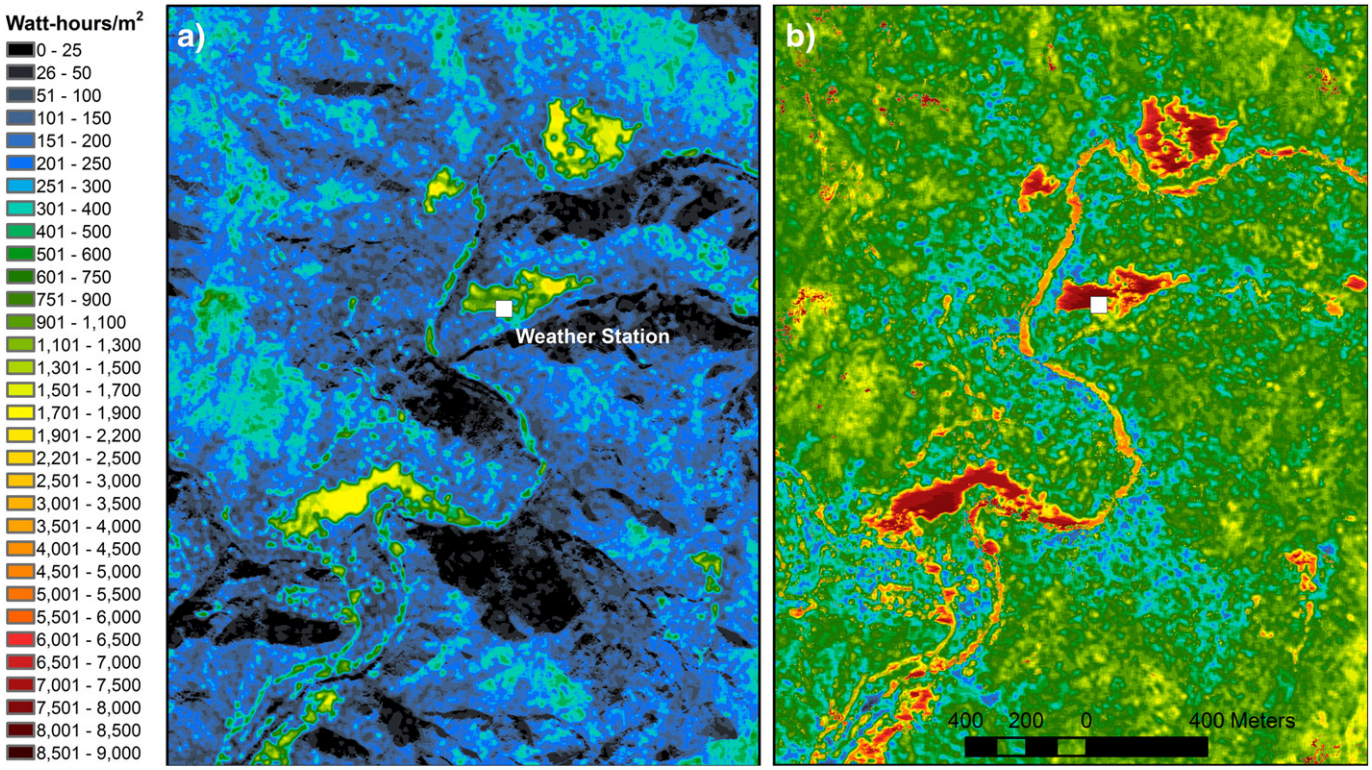

Fig. 10. SSR output a) winter solstice (Dec. 21), b) summer solstice (June 22).

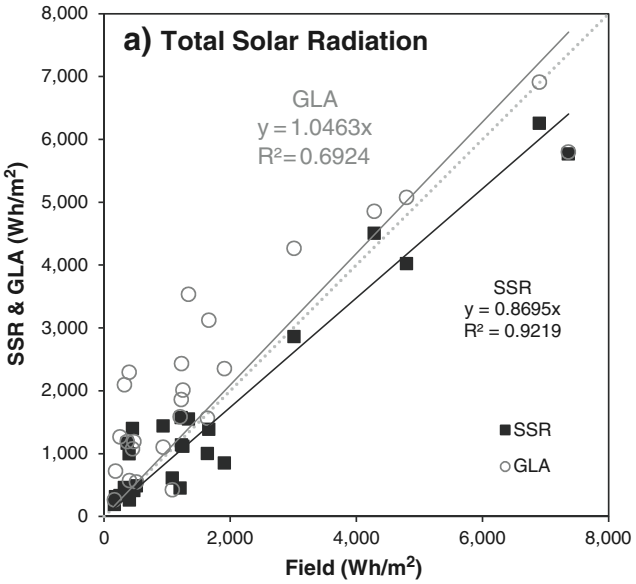

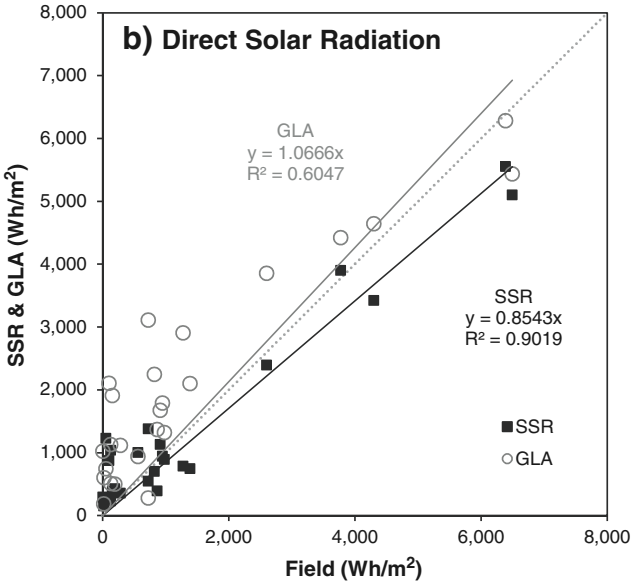

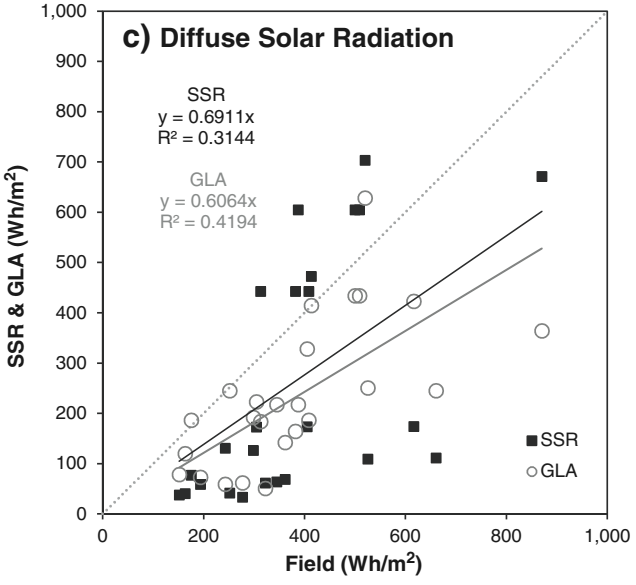

was mounted on a digital SLR (Nikon D200) and a bubble level was used to vertically center the camera. A Trimble GeoXT GPS unit was used to determine location. A compass was used to orient a north–south marker on the initial photograph. We then removed the marker and took a second photograph. The initial photograph was used to register (orient) the second photograph. The second photograph was processed and analyzed with Gap Light Analyzer software. GLA calculates the proportion of the sky visible in the photo. From the percentage canopy openness, GLA then models sunlight passing over the location for a particular day of year. The outputs are percent canopy openness, below-canopy (transmitted) direct, diffuse, and total solar radiation.

3. Results & discussion

SSR and Gap Light Analyzer exhibit a similar linear relationship with our pyranometer data, and both models predict similar total solar radiation flux across the range of canopy openness. Both do an excellent job capturing the direct radiation, but have a lower predictive value for diffuse radiation. SSR, however, can predict light regimes at watershed scales with resolutions equivalent to GLA or pyranometer point measurements (Fig. 10, Animation 1). This avoids the errors involved in upscaling point data to the watershed scale and makes possible high resolution modeling of light dependent watershed processes.

3.1. Comparison with pyranometer measurements

SSR total solar radiation predictions match pyranometer measurements well ($R^2 = 0.92$), although it consistently underestimates light levels (Fig. 11a). Direct solar radiation dominates that result, having similar values (Fig.11b). Low light conditions in heavily vegetated areas are a major source of error. This may be as much a measurement issue as a modeling issue. The lower the insolation level, the larger role a single sun fleck can play in the total radiation input. Forest edge is also a key source of error ($0.18 < LPI < 0.40$).

Both GLA and SSR had difficulty predicting diffuse radiation (Fig. 11c). This is unsurprising as diffuse radiation is difficult to model and the light levels are very low. Other attempts at using LiDAR for subcanopy shade modeling only modeled direct radiation and did not try to include diffuse (Lee et al., 2009; Mücke & Hollaus, 2011; Musselman et al., 2013). SSR shows split behavior due to having two sub-models. Values <300 Wh/m^2 come from the Understory sub-model and show broad scatter when compared to pyranometer measurements. Values >300 Wh/m^2 come from the Gap sub-model and match pyranometer measurements. This should be a target for improvement in subcanopy modeling, especially since our measurements showed diffuse to be 50%–100% of subcanopy insolation in under dense canopy. In addition, good modeling of diffuse radiation will allow practical modeling of real-sky conditions, because cloudy days increase diffuse radiation considerably, even when total radiation is lower.

3.2. Light penetration index as a measure of canopy openness

For applications related to vegetation structure, LPI can stand on its own as a method to assess canopy openness at the watershed scale. Gap Light Analyzer's canopy openness and LPI are well correlated ($R = 0.88$, $p << 0.001$, $n = 25$, Fig. 12) across a range of vegetation densities. Their methods are very different, which will cause divergence in very open areas. Dense low vegetation will cause LPI to show low openness even on a flat plane, while GLA will show 100% at the same location. A bare rock outcropping in a valley will be 1.0 on LPI index while GLA will show significant constraint due to the visual obstruction of the

Fig. 11. Relationships between field measurements of solar radiation, point estimates from Gap Light Analysis (spherical photography at given points), open circles; and predictions from the Subsurface Radiation model (filled squares) for a) total, b) direct, and c) diffuse radiation.

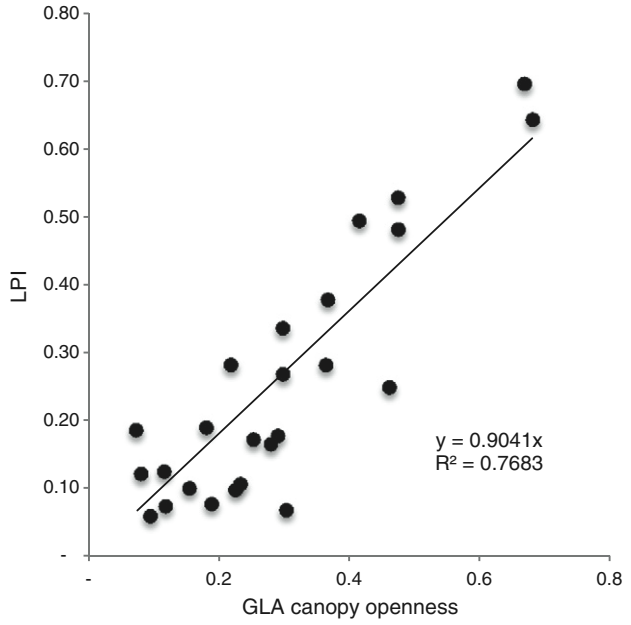

Fig. 12. LPI vs. GLA canopy openness.

rock hillslope. Nonetheless, as with SSR,LPI provides a way to assess canopy openness across entire watersheds without extensive field surveys, as has been pointed out by (Barilotti, Sepic, Abramo, & Crosilla, 2007).

3.3. Comparison with other efforts using LiDAR

There have been several efforts in recent years to capitalize on LiDAR for use in vegetative light modeling (Lee et al., 2009; Mücke & Hollaus, 2011; Musselman et al., 2013). All of these have focused on shadow modeling using voxels (volumetric pixels). The advantage of voxel modeling is that shadowing can be modeled for each time-step through a single day. In relatively open areas this provides much better resolution than SSR. There are several weaknesses, however, which our approach is well suited to address. First, most voxel-based calculations remove the most important part of the LiDAR dataset, the ground hit. Ground hits provide verification that light penetrated the vegetation reaching the understory floor. Second, as vegetation gets denser, LiDAR loses resolution in the lower canopy as the laser hits are blocked in the upper canopy. With dense vegetation, voxel shading will over-estimate light penetration at low angles due to an absence of hits near the ground. Third, computationally, it is not clear how scalable voxel based calculations are. Current efforts have been on the scale of 150 m × 250 m (Mücke & Hollaus, 2011) to 800 m × 800 m (Musselman et al., 2013). SSR runs on scales an order of magnitude larger (8000 m × 8000 m). Finally, SSR integrates topographic shading with the vegetative shading within an insolation model, where current voxel methods are modeling vegetation shading only.

4. Conclusions

The SSR model presented here estimates ground and stream surface level solar radiation for entire watersheds. It couples r.sun, a GIS based light model with orographic shading, with LPI which accounts for radiative transfer through vegetation. We validated SSR with direct and indirect measurements. SSR's estimates match the resolution quality of the best current point estimation techniques. It does so, however, at watershed scale, enabling high resolution modeling of light-dependent processes. SSR estimates light in areas with little to no field measurement as long as the area has LiDAR coverage. We validated the model with only partial calibration, providing a proof of concept. The model was developed in GRASSGIS, but the basic approach, could be used with other GIS-based solar models. By increasing the spatial and temporal scope and resolution of light data, our model will be useful for investigating the ecology, hydrology, and biogeochemistry of heavily vegetated watersheds.

Acknowledgments

This research was funded by the National Science Foundation's National Center for Earth-surface Dynamics (EAR-0120914), and the Eel River Critical Zone Observatory (EAR-1331940). LiDAR was flown by the NSF National Center for Airborne Laser Mapping. We would like to thank Graham Law and Charles Post for technical assistance with photography; the University of California Natural Reserve System and the Heath and Marjorie Angelo Coast Range Reserve and its steward, Peter Steel for providing a protected research site for this work; and the Saint Anthony Falls Laboratory (SAFL) at the University of Minnesota for use of their compute-workstations.

Appendix A. Supplementary data

Supplementary data associated with this article can be found in the online version, at http://dx.doi.org/10.1016/j.rse.2014.01.028. These data include Google map of the most important areas described in this article.

References

Anderson, M. C. (1964). Studies of the woodland light climate: I. The photographic computation of light conditions. *Journal of Ecology*, *27–41*.
Anderson, J., Martin, M. E., Smith, M. -L., et al. (2006). The use of waveform lidar to measure northern temperate mixed conifer and deciduous forest structure in New Hampshire. *Remote Sensing of Environment*, *105*(3), 248–261. http://dx.doi.org/10.1016/j.rse.2006.07.001.
Archibold, O. W., & Ripley, E. A. (2004). Assessment of seasonal change in a young aspen (*Populus tremuloides* Michx.) canopy using digital imagery. *Applied Geography*, *24*(1), 77–95. http://dx.doi.org/10.1016/j.apgeog.2003.11.001.
Axelsson, P. (1999). Processing of laser scanner data—Algorithms and applications. *ISPRS Journal of Photogrammetry and Remote Sensing*, *54*(2–3), 138–147. http://dx.doi.org/10.1016/S0924-2716(99)00008-8.
Barilotti, A. (2006). LAI determination in forestry ecosystem by LiDAR data analysis. *3D Remote Sensing in Forestry Conference 2006* (pp. 1–17).
Barilotti, A., Sepic, F., Abramo, E., & Crosilla, F. (2007). Improving the morphological analysis for tree extraction: A dynamic approach to lidar data. *ISPRS Workshop on Laser Scanning 2007* (pp. 1–6).
Boudreau, J., Nelson, R., Margolis, H., Beaudoin, A., Guindon, L., & Kimes, D. (2008). Regional aboveground forest biomass using airborne and spaceborne LiDAR in Québec. *Remote Sensing of Environment*, *112*(10), 3876–3890. http://dx.doi.org/10.1016/j.rse.2008.06.003.
Canham, C. D. (1988). An index for understory light levels in and around canopy gaps. *Ecology*, *69*(5), 1634–1638.
Chazdon, R. L., & Field, C. B. (1987). Photographic estimation of photosynthetically active radiation: Evaluation of a computerized technique. *Oecologia*, *73*(4), 525–532.
Chazdon, R. L., & Pearcy, R. W. (1991). The importance of sunflecks for forest understory plants. *BioScience*, *41*(11), 760–766.
Chazdon, R. L., Williams, K., & Field, C. B. (1988). Interactions between crown structure and light environment in five rain forest Piper species. *American Journal of Botany*, *1459–1471*.
Dozier, J., & Frew, J. (1990). Rapid calculation of terrain parameters for radiation modeling from digital elevation data. *IEEE Transactions on Geoscience and Remote Sensing*, *28*(5), 963–969.
Drake, J. B., Dubayah, R. O., Knox, R. G., Clark, D. B., & Blair, J. B. (2002). Sensitivity of large-footprint lidar to canopy structure and biomass in a neotropical rainforest. *Remote Sensing of Environment*, *81*(2), 378–392.
Ehleringer, J. R., Field, C. B., Lin, Z., & Kuo, C. (1986). Leaf carbon isotope and mineral composition in subtropical plants along an irradiance cline. *Oecologia*, *70*(4), 520–526.
Evans, G. C., & Coombe, D. E. (1959). Hemispherical and woodland canopy photography and the light climate. *Journal of Ecology*, *103–113*.
Falkowski, P. G., & LaRoche, J. (2004). Acclimation to spectral irradiance in algae. *Journal of Phycology*, *27*, 8–14.
Finlay, J. C. (2011). Stream size and human influences on ecosystem production in river networks. *Ecosphere*, *2*(8). http://dx.doi.org/10.1890/ES11-00071.1 (art87).
Frazer, G. W., & Canham, C. D. (Eds.). (1999). *GLA 2.0* (Retrieved December 11, 2012, from http://www.rem.sfu.ca/forestry/downloads/gap_light_analyzer.htm).
Frazer, G. W., Fournier, R. A., Trofymow, J. A., & Hall, R. J. (2001). A comparison of digital and film fisheye photography for analysis of forest canopy structure and gap light transmission. *Agricultural and Forest Meteorology*, *109*(4), 249–263.

Fu, P., & Rich, P.M. (2000). *A geometric solar radiation model and its applications in agriculture and, forestry, 357–364.*

Gendron, F., Messier, C., & Comeau, P. G. (1998). Comparison of various methods for estimating the mean growing season percent photosynthetic photon flux density in forests. *Agricultural and Forest Meteorology*, *92*(1), 55–70.

Glazer, A. N. (1985). Light harvesting by phycobilisomes. *Annual Review of Biophysics and Biophysical Chemistry*, *14*, 47–77. http://dx.doi.org/10.1146/annurev.bb.14.060185.000403.

Hardy, J. P., Melloh, R., Koenig, G., et al. (2004). Solar radiation transmission through conifer canopies. *Agricultural and Forest Meteorology*, *126*(3–4), 257–270. http://dx.doi.org/10.1016/j.agrformet.2004.06.012.

Helioclim (2011). Helioclim. Retrieved January 28, 2012, from. http://www.helioclim.org

Hill, W. R. (1996). Effects of light. In R. J. Stevenson, M. L. Bothwell, & R. L. Lowe (Eds.), *Algal Ecology* (pp. 121–148). New York, NY: Academic Press.

Hofierka, J., & Suri, M. (2002). The solar radiation model for Open source GIS: Implementation and applications. *Open source GIS — GRASS users conference 2002*.

Hudak, A. T., Evans, J. S., & Smith, A.M. S. (2009). *LiDAR utility for natural resource managers, 1–18. http://dx.doi.org/10.3390/rs1040934.*

Hurtt, G. C., Dubayah, R., Drake, J., et al. (2004). Beyond potential vegetation: combining lidar data and a height-structured model for carbon studies. *Ecological Applications*, *14*(3), 873–883.

Hyde, P., Dubayah, R., Walker, W., Blair, J. B., Hofton, M., & Hunsaker, C. (2006). Mapping forest structure for wildlife habitat analysis using multi-sensor (LiDAR, SAR/InSAR, ETM+, Quickbird) synergy. *Remote Sensing of Environment*, *102*(1), 63–73.

Julian, J. P., Stanley, E. H., & Doyle, M. W. (2008). Basin-scale consequences of agricultural land use on benthic light availability and primary production along a sixth-order temperate river. *Ecosystems*, *11*(7), 1091–1105. http://dx.doi.org/10.1007/s10021-008-9181-9.

Lakso, A. N. (1980). Correlations of fisheye photography to canopy structure, light climate, and biological responses to light in apple trees. *Journal of the American Society for Horticultural Science*, *105*(1), 43–46.

Lee, H., Slatton, K. C., Roth, B. E., & Cropper, W. P. (2009). Prediction of forest canopy light interception using three-dimensional airborne LiDAR data. *International Journal of Remote Sensing*, *30*(1), 189–207. http://dx.doi.org/10.1080/01431160802261171.

Lefsky, M.A., Cohen, W. B., Acker, S. A., Parker, G. G., Spies, T. A., & Harding, D. (1999). Lidar remote sensing of the canopy structure and biophysical properties of Douglas-fir western hemlock forests. *Remote Sensing of Environment*, *70*(3), 339–361.

Link, T. E., Marks, D., & Hardy, J. P. (2004). A deterministic method to characterize canopy radiative transfer properties. *Hydrological Processes*, *18*(18), 3583–3594. http://dx.doi.org/10.1002/hyp.5793.

Magnussen, S., & Boudewyn, P. (1998). Derivations of stand heights from airborne laser scanner data with canopy-based quantile estimators. *Canadian Journal of Forest Research*, *28*(7), 1016–1031.

MIDC (2013). *Measurement and instrumentation data center.* (Retrieved March 29, 2013, from http://www.nrel.gov/hsu/).

Mücke, W., & Hollaus, M. (2011). Modelling light conditions in forests using airborne laser scanning data. *Silvilaser, 2011*.

Musselman, K. N., Margulis, S. A., & Molotch, N.P. (2013). Estimation of solar direct beam transmittance of conifer canopies from airborne LiDAR. *Remote Sensing of Environment*, *136*(C), 402–415. http://dx.doi.org/10.1016/j.rse.2013.05.021.

Næsset, E., & Gobakken, T. (2008). Estimation of above- and below-ground biomass across regions of the boreal forest zone using airborne laser. *Remote Sensing of Environment*, *112*(6), 3079–3090. http://dx.doi.org/10.1016/j.rse.2008.03.004.

Nęsset, E. (1997). Estimating timber volume of forest stands using airborne laser scanner data. *Remote Sensing of Environment*, *61*(2), 246–253.

Pearcy, R. W. (1983). The light environment and growth of C 3 and C 4 tree species in the understory of a Hawaiian forest. *Oecologia*, *58*(1), 19–25.

Pearcy, R. W. (1990). Sunflecks and photosynthesis in plant canopies. *Annual Review of Plant Biology*, *41*(1), 421–453.

Pomeroy, J., Ellis, C., & Rowlands, A. (2008). Spatial variability of shortwave irradiance for snowmelt in forests. *Journal of Hydrometeorology*, *9*(6), 1482–1490. http://dx.doi.org/10.1175/2008JHM867.1.

Reid, T. D., Essery, R. L. H., Rutter, N., & King, M. (2013). Data-driven modelling of shortwave radiation transfer to snow through boreal birch and conifer canopies. *Hydrological Processes*. http://dx.doi.org/10.1002/hyp.9849 (n/a–n/a.).

Remund, J., Wald, L., LefÈvre, M., Ranchin, T., & Page, J. (2003). Worldwide Linke turbidity information. *Proceedings of ISES Solar World Congress 2003, CD-ROM*.

Rich, P.M. (1990). *A manual for analysis of hemispherical canopy photography.* Los Alamos, N.M.: Los Alamos National Laboratory, 80.

Shapiro, M. (Ed.). (2010). *r.neighbors* (Retrieved May 26, 2012, from http://grass.osgeo.org/grass64/manuals/r.neighbors.html).

Shapiro, M., & Clements, G. (Eds.). (2010). *r.mapcalc* (Retrieved May 26, 2012, from http://grass.osgeo.org/grass64/manuals/r.mapcalc.html).

Slatton, K. C., Carter, W. E., Shrestha, R. L., & Dietrich, W. (2007). Airborne Laser Swath Mapping: Achieving the resolution and accuracy required for geosurficial research. *Geophysical Research Letters*, *34*(23), L23S10. http://dx.doi.org/10.1029/2007GL031939.

Solpos (2012). *Solpos: Solar position software.* (Retrieved July 15, 2012, from http://www.nrel.gov/midc/solpos).

Šúri, M., & Hofierka, J. (2004). A new GIS-based solar radiation model and its application to photovoltaic assessments. *Transactions in GIS*, *8*(2), 175–190.

Suttle, K. B., Thomsen, M.A., & Power, M. E. (2007). Species interactions reverse grassland responses to changing climate. *Science*, *315*(5812), 640–642. http://dx.doi.org/10.1126/science.1136401.

Vignola, F., Stoffel, T., & Michalsky, J. (2012). *Solar and infrared radiation measurements* (1st ed). Boca Raton, FL: CRC Press (Retrieved from http://www.crcpress.com/product/isbn/9781439851890).

Wasser, L., Day, R., Chasmer, L., & Taylor, A. (2013). Influence of vegetation structure on lidar-derived canopy height and fractional cover in forested riparian buffers during leaf-off and leaf-on conditions. In G. J. -P.Schumann (Ed.), *PLoS One*, *8*(1), e54776. http://dx.doi.org/10.1371/journal.pone.0054776.t008.